Hindawi
Structural Control and Health Monitoring
Volume 2023, Article ID 1981892, 18 pages
https://doi.org/10.1155/2023/1981892

Research Article

Microwave Structural Health Monitoring of the Grouted Connection of a Monopile-Based Offshore Wind Turbine: Fatigue Testing Using a Scaled Laboratory Demonstrator

Thomas Maetz,[1] **Jonas Kappel**,[2] **Marcel Wiemann**,[2] **Dirk Bergmannshoff**,[3] **Manfred Hägelen**,[4] **Rainer Jetten**,[4] **Matthias Schmidt**,[3] **Johannes Käsgen**,[3] **Marco Jackel**,[3] **Jochen Moll**,[1] **Peter Kraemer**,[2] **and Viktor Krozer**[1]

[1]*Department of Physics, Goethe University Frankfurt, Frankfurt am Main, Germany*
[2]*Department of Mechanical Engineering, University of Siegen, Siegen, Germany*
[3]*Fraunhofer Institute for Structural Durability and System Reliability LBF, Darmstadt, Germany*
[4]*IMST GmbH, Kamp-Lintfort, Germany*

Correspondence should be addressed to Thomas Maetz; maetz@physik.uni-frankfurt.de and Jochen Moll; moll@physik.uni-frankfurt.de

Received 31 July 2023; Revised 7 November 2023; Accepted 27 November 2023; Published 13 December 2023

Academic Editor: Fabio Casciati

Offshore wind turbines play a significant role in the expansion of clean and renewable energy. However, their exposure to harsh marine environments and dynamic loading conditions poses significant challenges to their structural integrity. In particular, the grouted connection, serving as the crucial interface between the monopile and the transition piece, is susceptible to cracking and particle washout that can lead to destabilizing grout erosion over time. In this paper, we propose a microwave structural health monitoring (SHM) approach for damage detection in grouted connections based on a stepped-frequency continuous wave radar. The methodology exploits ultra-wideband (UWB) electromagnetic wave propagation in the frequency range from 100 MHz to 2 GHz, where the microwaves propagate along the concrete-type dielectric material guided by the surrounding steel cylinders. For the proof of concept, a scaled laboratory demonstrator was built that realistically models the dynamic loading experienced by a full-scale monopile. The structure was equipped with an UWB radar system using two transmitting and three receiving antennas directly coupled to the grout. For validation, a large number of other sensors, i.e., accelerometers, strain gauges, and acoustic emission sensors have also been installed and measured synchronously during the fatigue test. It is demonstrated here that the proposed SHM methodology offers a nondestructive and real-time method for assessing the structural integrity of the grouted connection directly, actively, and automatically. This has the potential to support predictive maintenance activities in the future.

1. Introduction

Offshore wind energy has emerged as a vital source of renewable power in recent years. In 2022, the nominal global offshore wind power capacity increased by 8.8 GW, bringing the total capacity to 64.3 GW [1]. Forecasts indicate that the market will grow significantly between 2023 and 2027, with an expected 130 GW to be added worldwide during this period. In Europe, the cumulative offshore wind capacity reached already 30 GW. The European Union (EU) has outlined in its offshore renewable energy strategy [2] that it aims to reach an installed capacity of at least 60 GW by 2030 and 300 GW by 2050.

As offshore wind farms grow in size, the need for robust monitoring systems increases as they help ensure the safety, reliability, and performance of offshore wind turbines, particularly with regard to foundation structures. The benefits of a structural health monitoring (SHM) system for the support structures of offshore wind turbines are summarized in [3], considering relevant failure modes.

The prevailing choices for offshore wind turbine foundations are monopiles [4]. After the monopile has been driven into the seabed, the transition piece with a larger diameter is placed on top with an overlap of several meters. The gap between both steel tubes is filled with high-performance grout, a special type of concrete, forming the grouted connection (see Figure 1). During the operation, the offshore wind turbine is subjected to harsh weather conditions and intense dynamic loads caused by wind and waves. It has been observed in [6] that the grouted joints are susceptible to cracking due to the large bending moments they experience. The presence of cracks enables the penetration of water, leading to the possibility of additional crack propagation [7] and erosion [8].

Tziavos [9] describes that, in September 2009, regular inspections of monopiles identified the slippage of numerous transition pieces by as much as 90 mm. The following examinations concluded that approximately 700 out of 1,000 monopiles across Europe had slipped significantly. A gap between grout and steel was detected at the top of some grouted joints and water ingress was evident in certain cases. The design practices for grouted connection on offshore wind turbines were consequently reevaluated. This highlights the importance of detecting any changes in the grouted connection as early as possible to ensure the stability of the offshore wind turbines. Therefore, methods are necessary that can provide continuous and nondestructive monitoring of the grouted connection during operation, ultimately establishing a SHM system.

In the field of SHM, the importance of speed, accuracy, and labor efficiency for the evaluation of vital structures was underscored by Shan et al. [10]. In recent years, a typical sensor configuration to monitor offshore wind foundations consists of acceleration, inclination, and strain sensors, to study vibration amplitudes, natural frequencies, and inclinations [11]. This approach is shown, for example, by Stuyts et al. [12] who consider accelerometers and fiber optical sensors for structural assessment of a wind turbine monopile. They also propose an earth pressure sensor as well as a piezo-resistive pressure sensor. Shan et al. [13] showed that damping ratios can be more sensitive to measurement noise and sensor allocation than modal frequencies. Liu et al. [14] analyzed acceleration and inclination sensors for the impact assessment of typhoon "In-fa" on the dynamic properties of monopile offshore wind turbines. On top, SCADA (supervisory control and data acquisition) data have been recorded along with the sensor data in order to correlate the measurements with the parameters of the wind turbine such as wind speed, wind direction, turbine yaw angle, and turbine power output [12].

On laboratory scale, Müller et al. [15] successfully demonstrated strain sensing via fiber Bragg gratings (FBGs) in a large-scale offshore wind turbine grouted connection specimen. In that work, damage sensitive features have been derived from the FBG signal responses using the Wigner–Ville distribution and energy spectral density. A large-scale laboratory experiment has also been studied by Häckell et al. [16] using inclination sensors and accelerometers. Other approaches for monitoring grouted connections are based on guided ultrasound waves [17] and electromechanical impedance spectroscopy [18].

Ground penetrating radar (GPR) is commonly used for the nondestructive testing (NDT) and monitoring of concrete structures such as bridge decks, beams, columns, slabs, and walls [19–22]. In many applications, the focus is on the analysis of reinforcements. Manual scanning by moving the radar antennas along the scanning object is frequently used, allowing for the detection and localization of embedded objects, such as rebars and cables. Depending on the radar system parameters (e.g., frequency and transmission power) and the material to be examined, the depth to which flaws can be detected varies. Under the conditions described in [23], the detection depth was determined to be up to 20 m at 100 MHz, up to 7 m at 270 MHz and up to 5 m at 400 MHz. There are commercial GPR scanners for the examination of steel-reinforced concrete parts [24–26]. Higher frequencies usually provide a higher resolution and reduced penetration depth while lower frequencies provide greater penetration depth with reduced resolution [27]. The successful application of GPR systems in NDT of concrete structures can be considered as a promising prior work to develop a microwave SHM system for grouted connections.

The novelty of this research includes the development and testing of a GPR system specifically designed for the continuous monitoring of grouted connections. A high radar sensitivity is achieved by using a stepped-frequency continuous wave (SFCW) radar design that supports a long measurement time, which enables a high dynamic range as well as low noise levels. Besides the advantages of SFCW radar systems for static scenarios, our approach has several advantages compared to existing nondestructive testing methods for grouted connections. Radar enables the direct, active, and automatic inspection of the grouted connection in offshore wind turbines. Typically, damage in these connections is inferred indirectly by examining operational parameters and measured loads. Methods such as acoustic emissions are passive measurements and therefore require a high uptime of the measurement system to not miss the relevant emissions. X-rays, ultrasound, and electromechanical impedance spectroscopy are direct measurements, but they have not yet been utilized automatically for grouted connections in offshore wind turbines, without the need for on-site personnel. Due to the limited accessibility to offshore wind energy turbines, given their distance from the coastline and variable weather conditions, only an automatic inspection method can operate continuously. For the installation of the radar system, only the inner part of the transition piece needs to be accessed. This location ensures good protection of the system from the harsh environment.

Initial results from the accompanying offshore installation have been presented in [5, 28]. The antennas of the GPR system are permanently attached to the grout structure so that relative changes between measurements from baseline conditions and measurements during the subsequent lifetime of the structure can be evaluated. To evaluate the radar systems damage detection performance, a large-scale fatigue experiment has been developed and

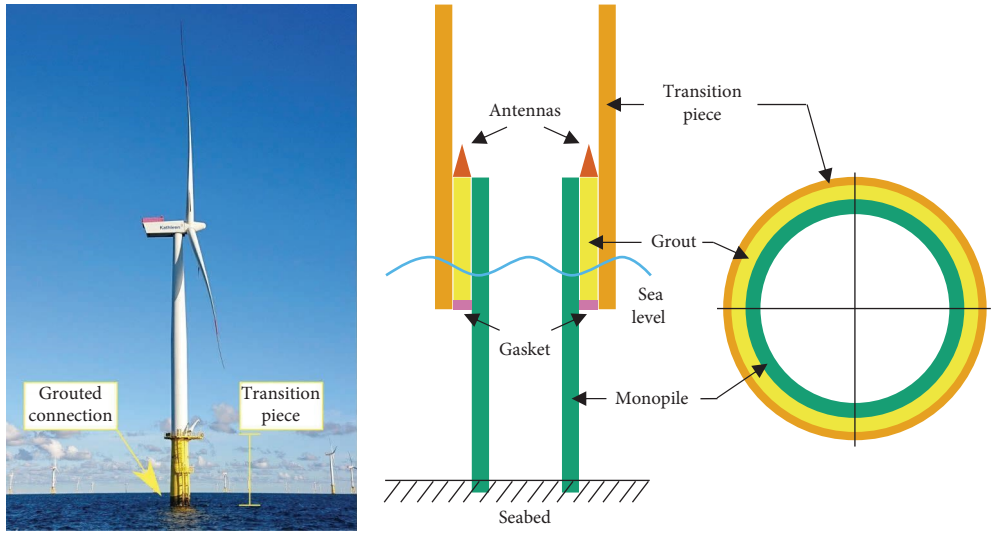

FIGURE 1: (a) Location of the grouted connection on a 3.6 MW offshore wind turbine [5]; (b) illustration of the grouted connection showing the application of the radar antennas on top of the grout.

implemented where the radar sensor (including two transmitting and three receiving antennas) have been installed. In addition to the radar system results, this study incorporates measurements gathered from the testing system and other synchronized sensors, such as cameras, accelerometers, strain gauges, and acoustic emission sensors.

2. Materials and Methods

2.1. Design of the Scaled Laboratory Demonstrator. To assess the SHM system performance under controlled laboratory conditions, a scaled laboratory demonstrator was constructed (Figure 2(a)) for accelerated life cycle testing under realistic operational loads but without environmental influences. Therefore, the design of the demonstrator focused on the dimensions of a grouted connection at nearly full-scale and the capability to apply realistic load scenarios. This enables the application of fatigue tests and structural dynamic tests and provides adequate space for radar antenna placement during the tests, respectively. Since the radar system monitors the grouted connection, it is essential to ensure that any damage, such as cracks, occurs only in the grout during the fatigue tests. Thus, the design and calculation of the structural strength were carried out using the finite element method (FEM). This optimization process aimed to prevent critical stresses from occurring in other parts of the laboratory demonstrator structure (see Figure 2(b)).

The structure consists of an inner tube (monopile) which measures 813 mm in outer diameter and an outer tube (transition piece) with an inner diameter of 1093 mm. Furthermore, rectangular shear keys with a cross section of 10 mm × 10 mm (see Figure 3(a)) have been welded to both the inner and outer tubes. To facilitate access to the grout with a radial thickness of 140 mm and a height of 1000 mm, the arrangement of the tubes was reversed so that the monopile is facing upwards and the transition piece is fastened to the clamping field. This configuration exposes the upper area of the grouted connection entirely, to give easy access for radar antenna installation and visual inspection of the grouted joint. Additionally, this also provides access to the inner area of the monopile through a ladder. The grout's bottom is accessible to water and inspection via a 150 mm gap. The grouted connection utilized a total of 900 kg of PAGEL HF10 high-strength grout [29] to fill the gap between both steel tubes (Figure 3(a)). During several months of curing, the sensor setup, consisting of radar antennas and other sensors, was installed (Figure 3(b)).

Three hydraulic cylinders are used to apply fatigue loads to the monopile. These forces are then transmitted through the grouted connection to the transition piece and the clamping field. In real wind turbines, the main loading on the grouted connection arises from bending and torsional moments caused by the wind forces at the rotor's height. To simulate the bending moments, the test rig employs two axial 400 kN hydraulic cylinders. Additionally, the shear force is applied by a radial cylinder with a capacity of 100 kN.

Structural dynamic tests were conducted using an electrodynamic shaker (see Figure 4), equipped with an additional excitation mass that was mounted at the top of the laboratory demonstrator to provide the required broadband excitation: sweep sine and random noise in the frequency range from 5 Hz to 1000 Hz.

2.2. Description of the Radar Sensor System. The radar sensor operates from 100 MHz to 2 GHz in a stepped frequency mode. It allows the simultaneous connection of 2 transmit (Tx) and 3 receive antennas (Rx), alongside a BME280 environmental sensor [30] which is connected to the radar sensor using the serial communication bus Inter-Integrated Circuit (I^2C). The air temperature, air humidity, air pressure,

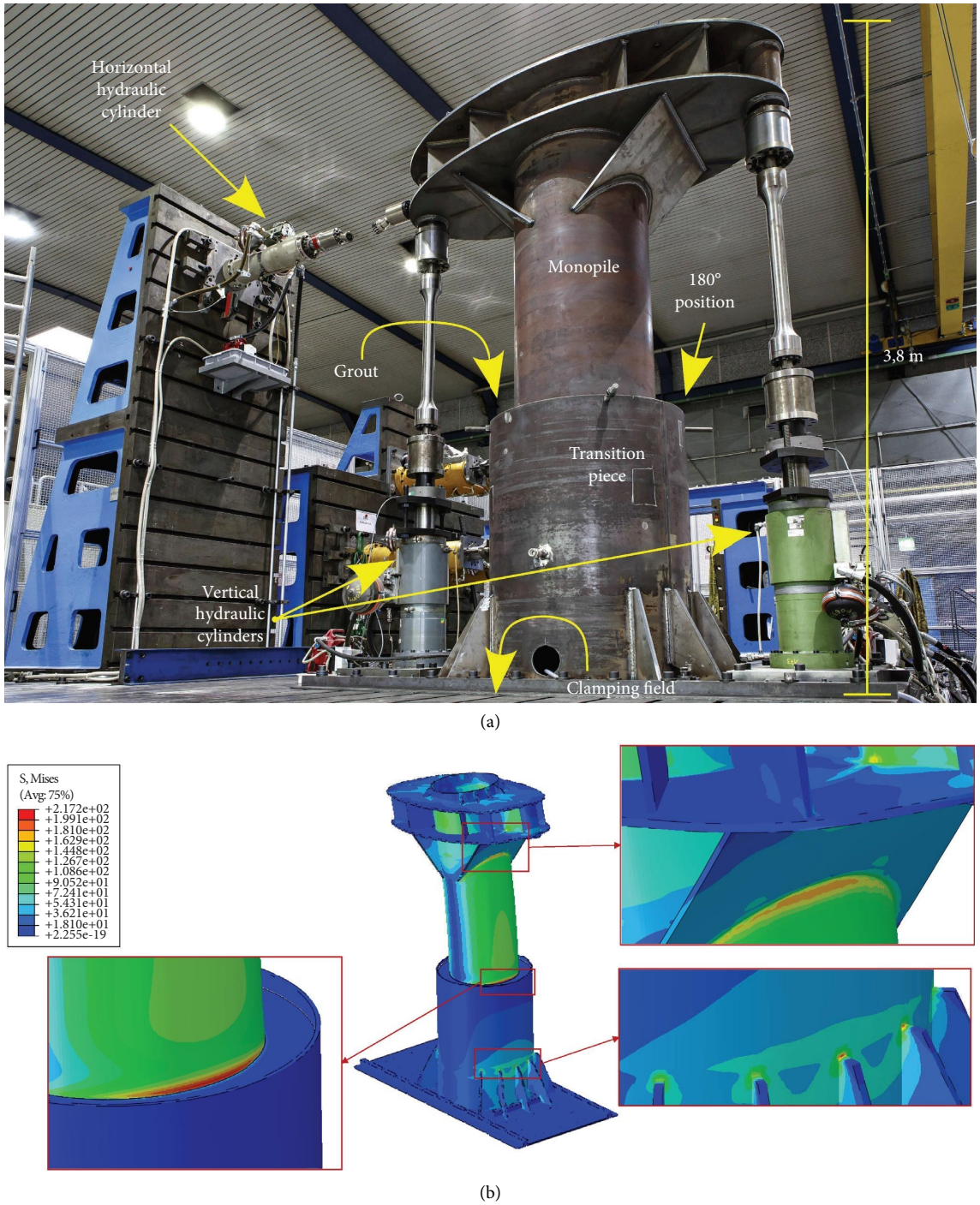

FIGURE 2: (a) Overview of the laboratory demonstrator with labels of its main components; (b) results of the finite element analysis showing the one of the areas with the highest stress in red at the 180° position in the grouted region.

and several internal temperatures are recorded. To simplify installation and operation, a single cable provides both power and data connectivity to the sensor via Power-over-Ethernet (PoE). To enable visual detection of fatigue damage and monitoring the laboratory, three cameras are also connected via PoE. The data collected by all sensors and cameras are first stored locally before being sent to servers in Frankfurt and Siegen for redundant storage and further analysis. Figure 5 shows the radar sensor for illustration purposes with an open housing cover. Table 1 lists its main characteristics.

The radar sensor is attached to the outer metal tube using a 3D printed mounting frame that securely hooks onto the tube's edge and is held in place by a screw. At the bottom, the sensor is connected to the tube by a strong magnet. To dampen the vibrations transmitted from the metal tube to

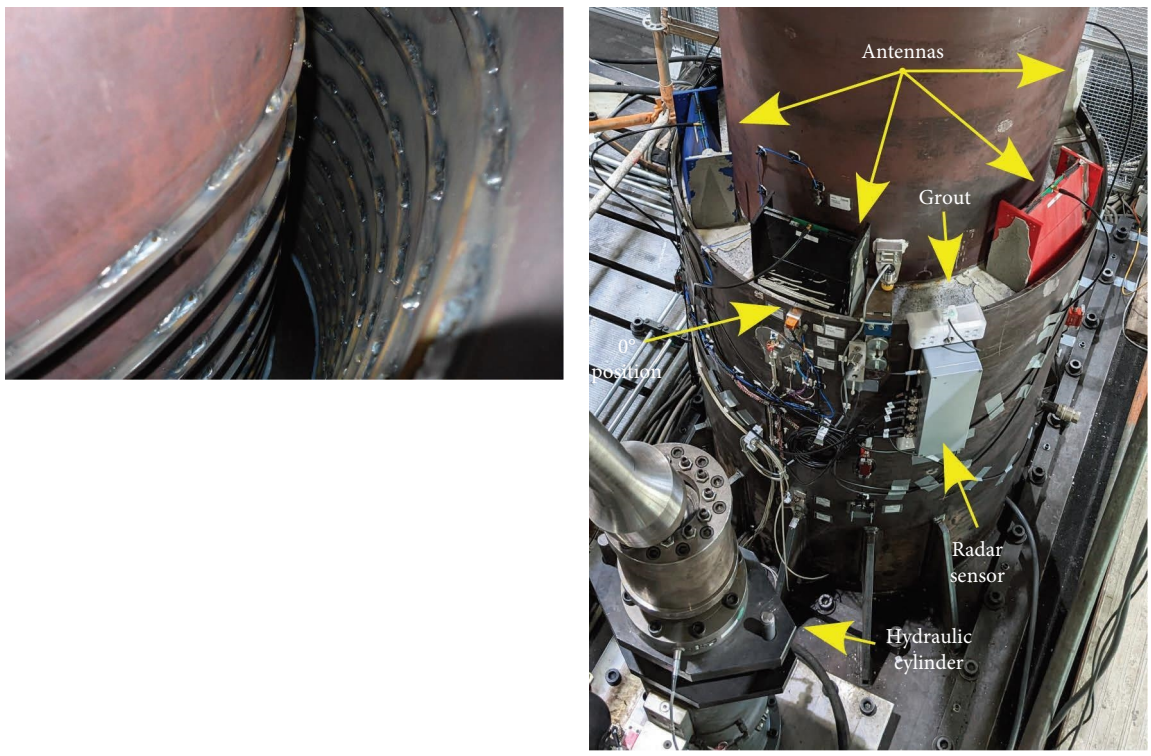

(a) (b)

Figure 3: (a) Gap between the metal tubes with shear keys that is subsequently filled with grout; (b) radar sensor mounted on the outer metallic tube together with the antennas directly coupled to the grout from the top. Additionally, a hydraulic cylinder and other sensors are shown.

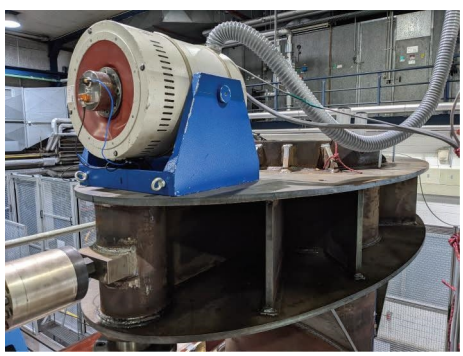

Figure 4: Electrodynamic shaker used for dynamic testing during the fatigue test.

the radar sensor, a combination of PETG (polyethylene terephthalate glycol) and TPU (thermoplastic polyurethane) plastics were used for the 3D printed components.

Each transmit and receive antenna consists of a pair of flame retardant 4 (FR-4) printed circuit boards affixed to 3D printed PETG components using polyamide screws and nuts. These PCBs are soldered to a SMA connector, enabling the antenna's connection to the radar sensor through a coaxial cable of 2 meters length. The soldering area is protected by liquid rubber before the antenna is filled with PAGEL HF10 grout during the manufacturing process. This means that the same grout material is used for the antenna design and the grouted connection of the test rig for the large-scale fatigue experiment.

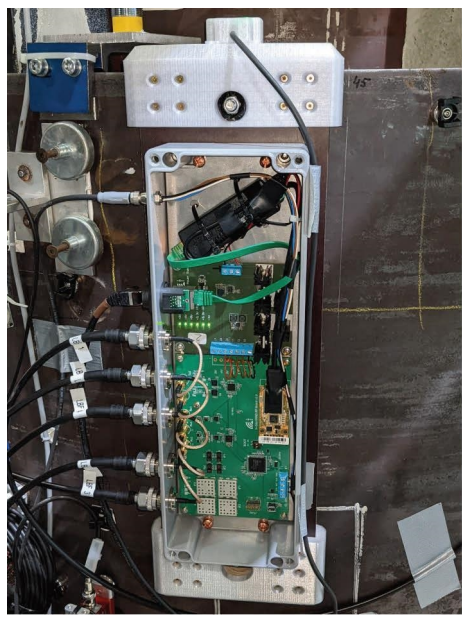

Figure 5: Radar system with open housing cover.

To install the antennas, the area was marked by self-adhesive foam on the grouted connection, shaping it into the form of a rectangle. Then, a thin layer of new PAGEL HF10 grout is poured onto the existing grouted joint within this delineated space. Subsequently, the antenna is positioned on this newly laid foundation.

Table 1: Operating parameters of the radar sensor.

Parameter or component	Value	Comment
Housing	IP66	Robust, dust-proof, and waterproof
Interface	Ethernet	High data rates over long distances
Power supply	PoE	Common cable for interface and power supply
Power consumption	~10 W	Limited by the PoE splitter used
Cooling	Passive	No active cooling (fan) required
Minimum frequency	~100 MHz	
Maximum frequency	2 GHz	
Max. transmission power	1 W	Reducible by ~40 dB
HF connector	*N*-female	Robust
Impedance	50 Ω	For all transmission and reception channels
Transmission channels	2	Operation individually or in parallel
Receive channels	3	Simultaneous reception and evaluation
Weight	3 kg	Without cable and environmental sensor

The positioning of each antenna on the grouted connection is depicted in Figure 6 and summarized in Table 2. Based on the finite element analysis (see Figure 2(b)), antennas Tx2 and Rx2 were positioned equidistantly from one of the areas with the highest stress, at the angular position 180°. This is the region where damage is most likely to occur. Antenna Tx1 was placed at the 0° position on top of the corresponding area on the opposite side that experiences the same loads. Antenna Rx3 was placed symmetrically between Tx2 and Tx1 so that the distance on the circumference to both is the same. Antenna Rx1 was placed asymmetrically by deliberately moving it closer to Tx1.

Figure 7 presents the measurements of the input reflection coefficient S_{11} obtained using a vector network analyzer for the antenna characterization. These measurements are depicted for two different structures: (a) a simplified structure discussed in [31], utilizing a Keysight M9807A vector network analyzer and (b) the final laboratory demonstrator structure, where a NanoVNA V2 Plus4 vector network analyzer was employed two months after the antennas were installed on the grouted connection. It is notable that the performance of the antennas slightly varies with the specific setup and the VNA used. Despite the variations, all antennas perform well within the desired frequency range in both configurations.

2.3. Description of the Measurement Protocol. Table 3 presents the comprehensive test program for the fatigue test, outlining the specific test parameters for a total of 72,000 cycles. Sinusoidal forces are used according to Table 3, whereas the forces of the two vertical cylinders are inversely phased to generate the targeted bending moment. The load is expressed as percentage relative to the maximum potential vertical force of 400 kN and the maximum potential horizontal force of 10 kN.

After several months of curing, initial reference measurements were taken with the grout in dry condition. On November 09 at 10:30 UTC, the water was filled to 450 mm, i.e., 300 mm above the bottom end of the grout. All tests presented below were conducted with the bottom area of the grouted connection in direct contact with water. This approach aims to replicate offshore conditions and enables the generation of realistic particle washout of the grout material.

To identify changes in the structural behavior of the demonstrator during the fatigue test, dynamic tests using sweep sine and random noise excitation were conducted after each load level using the electrodynamic shaker shown in Figure 4. The results obtained from the dynamic tests were evaluated using modal analysis procedures to identify the trend of change considering eigenfrequencies, mode shapes, and damping properties. All dynamic tests were performed under identical loading conditions to exclude any other influences on the structural behavior.

2.4. Description of Radar Signal Processing. In order to analyze each radar measurement, the inverse fast Fourier transform (IFFT) is utilized to convert the measured frequency domain data to the time domain. The absolute value is then calculated to obtain real values from the complex data. These real values form a single column in Figure 8(a). The columns represent different time points captured during the measurement period, using a specific antenna combination (where Tx2 is a transmitter and Rx2 is a receiver). To condense each column into a scalar metric, the root mean square (RMS) is computed for each signal (see (1)) as a widely used damage sensitive metric to identify trends in the radar data [32].

$$\mathrm{RMS} = \sqrt{\frac{1}{n}\sum_{i=1}^{n} x_i^2}, \tag{1}$$

Here, $x(t)$ describes the time-domain radar signal and n is the number of sampling points in that signal. The development of the RMS values over time is shown in Figure 8(b). To visualize the changes that occur throughout one day, the differential data can also be obtained by subtracting the first column in Figure 8(a) from all the other columns. This differential data are plotted in Figure 8(c). On the other hand, Figure 8(d) displays the ratio of the current RMS value of Figure 8(b) to the initial RMS value of the entire measurement period.

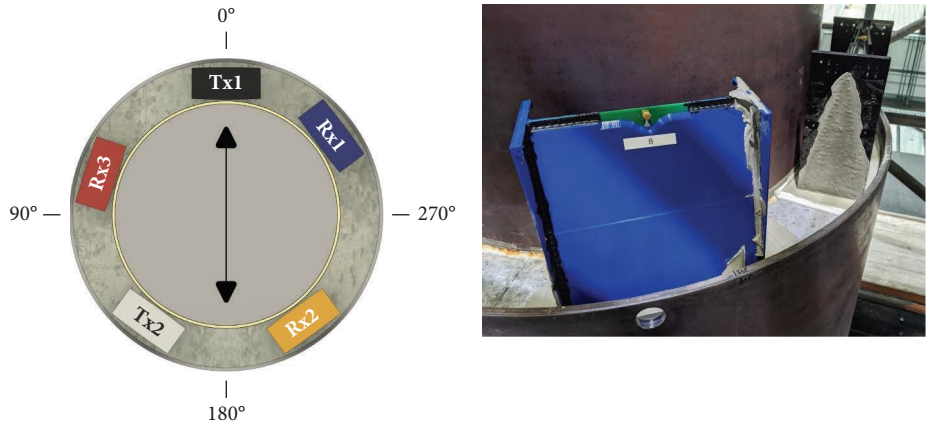

Figure 6: (a) Antenna placement on the grouted connection with an arrow indicating the load direction for bending; (b) two antennas installed on the grouted joint without coaxial cable.

Table 2: Antenna placement on the grouted connection.

Color	Cable length (m)	Channel	Angle at center (°)	Circumference at center (cm)
Black	2	Tx1	0	0.0
Red	2	Rx3	72	70.2
White	2	Tx2	144	140.5
Yellow	2	Rx2	216	210.7
Blue	2	Rx1	307	299.5

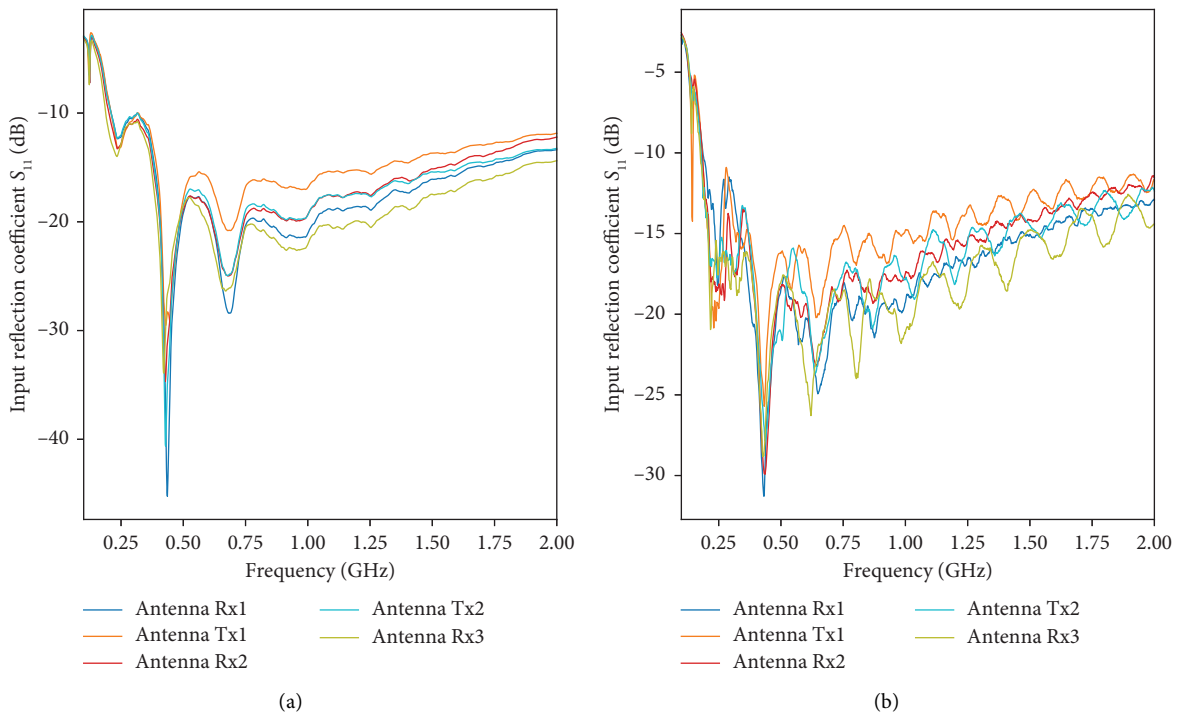

Figure 7: Input reflection coefficient S_{11} of all five antennas used in this study; (a) on a simplified structure described in [31] (using a Keysight M9807A vector network analyzer) and (b) on the final laboratory demonstrator structure (using a NanoVNA V2 Plus4 vector network analyzer).

Table 3: Procedure and test parameters for fatigue test.

Date	Load (%)	Load type	Force vert. (kN)	Force horiz. (kN)	Duration (h)	Frequency (Hz)	Cycles (Nr.)
November 14	10	Bending, shear	40	1	5	1	18,000
November 16	20	Bending, shear	80	2	5	1	18,000
November 18	40	Bending, shear	160	4	5	1	18,000
November 22	60	Bending, shear	240	6	5	1	18,000

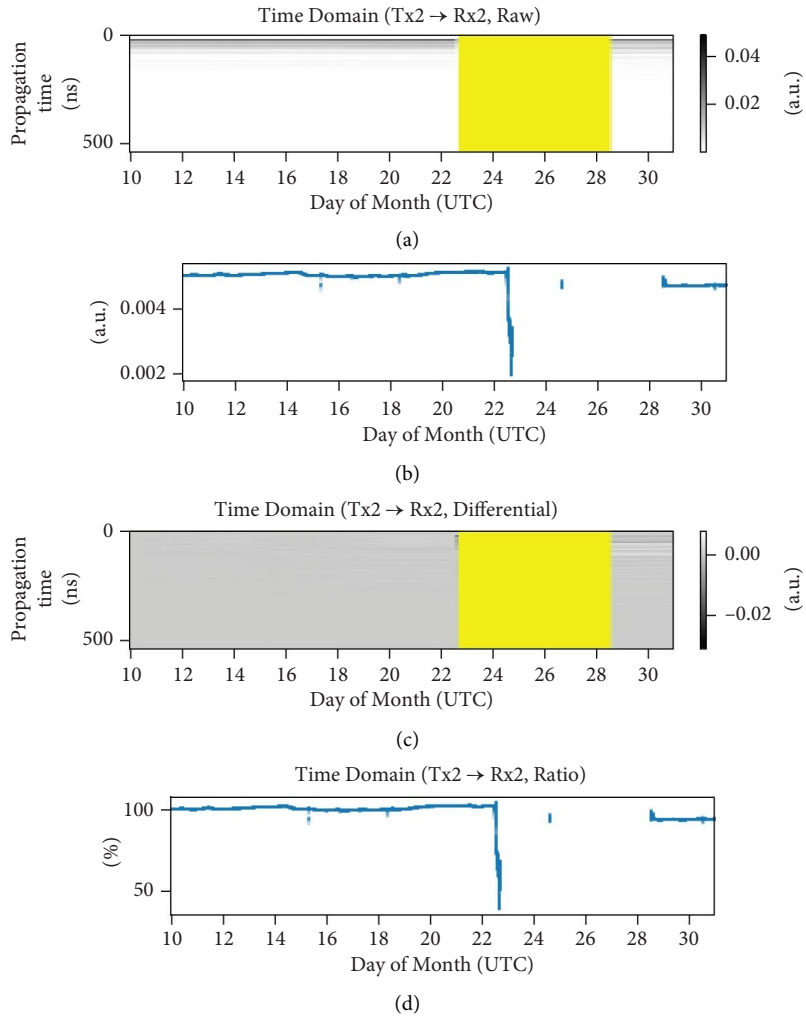

Figure 8: Radar signal processing (yellow indicates missing data): (a) absolute time domain data from one antenna combination (Tx2 as transmitter and Rx2 as receiver); (b) root mean square (RMS) of each column shown in (a); (c) differential time domain data calculated by subtracting the first column of all columns shown in (a); (d) ratio of the RMS in (b) compared to the initial RMS value in (b).

For the sake of simplicity, we will only consider the values shown in Figure 8(d) as a damage indicator in the radar plots that follow.

3. Results and Discussion

3.1. Documentation of Damage Evolution. During the fatigue tests, as the load levels increased, massive water leakage of several liters occurred on the top side of the grout. This leakage was accompanied by progressive cracking of the grout material. Due to the loads applied by the hydraulic cylinders the grout was partially crushed into smaller pieces and water was pumped upwards through the cracks causing a wash out of the pulverized grout material. The washed-out material was collected in containers (see Figure 9) for the top (a) and bottom (b) of the grouted connection after an inspection on December 6. The variation in appearance may be attributed to (a) being scraped and vacuumed when dry, while (b) was scraped when wet and then dried afterwards. It can be assumed that a total of approx. 9 kg of the grout material was washed out after the first revision (72,000 cycles), which corresponds to approx. 1% of the total grout material mass.

(a) (b)

Figure 9: Washed-out material (a) on the top and (b) on the bottom of the grouted connection. (a) Being scraped and vacuumed when dry; (b) being scraped while wet and subsequently dried.

Figure 10 exhibits the grouted connection after 72,000 cycles. The yellow arrow indicates the 180° position. Damage is visible in this area where the finite element analysis predicted one of the areas with the highest stress (refer to red colored area in Figure 2(b)).

Figure 11 illustrates the development of visual damage of the grout surface over time on a specific date (November 22) at two opposite sides of the demonstrator (90° and 270°). Immediately after the demonstrator was cured, small radial surface cracks became visible. At 12:09 UTC, a wet circumferential crack appeared at the 270° position, indicated by a yellow arrow. By 12:14 UTC, water could be seen escaping from one of the existing radial cracks at the 90° position. At 12:26 UTC, an increasing amount of water emerged from the cracks, filling the space above the grout until only the water surface was visible. By 15:27 UTC, most of the water had disappeared from the surface, although it remained wet. At 16:18 UTC, the surface had dried up further, and the radar measurement was stopped due to water entering the Ethernet port, which required the replacement of it afterwards. Due to the deposition of pulverized grout sediment, a fresh layer has been formed on the existing grout surface, giving it a smooth appearance. See video clip in the Supplementary Materials (available here) for a time-lapse sequence showing the development of the visible damage on November 22.

3.2. Analysis of Testing Machine Parameters. The hydraulic cylinders' force and displacement data were recorded in parallel to the SHM sensor system. To calculate the moment for further analysis, the values of one vertical cylinder were subtracted from the other. This subtraction helps cleaning the signals by eliminating the effect of the hydraulic cylinder heating up, which causes a drift in the displacement signal.

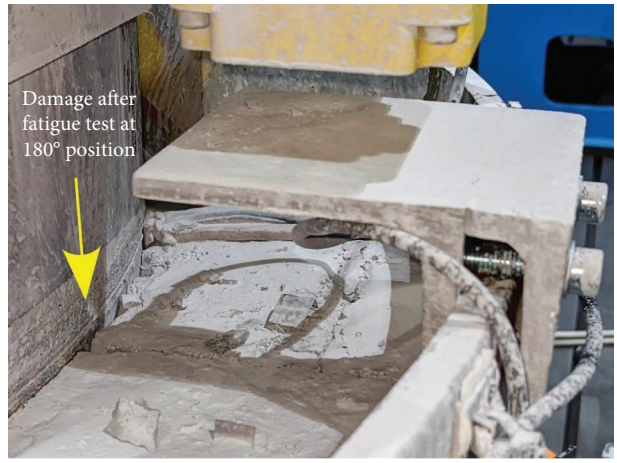

Figure 10: Grouted connection after 72,000 cycles of the fatigue test with one arrow indicating the 180° position with visible damage. The finite element analysis predicted one of the regions with the highest stress in this region (see red colored area in Figure 2(b)).

Next, the measured signal was divided at every second zero crossing point. Figure 12 displays the plot of the difference in force and displacement on the left side for the beginning and end of November 22. Even at this stage, it is noticeable that the displacement signal is not as well aligned with the force signal by the end of the day compared to the beginning. This misalignment becomes more apparent when the force/displacement is plotted on the right side for the specific times.

As explained in [33], an increase in area of the hysteresis loops indicates damage. The area represents the mechanical work of grinding the grout into smaller pieces and can be determined by calculating the integral over the force/displacement curve (see (2)).

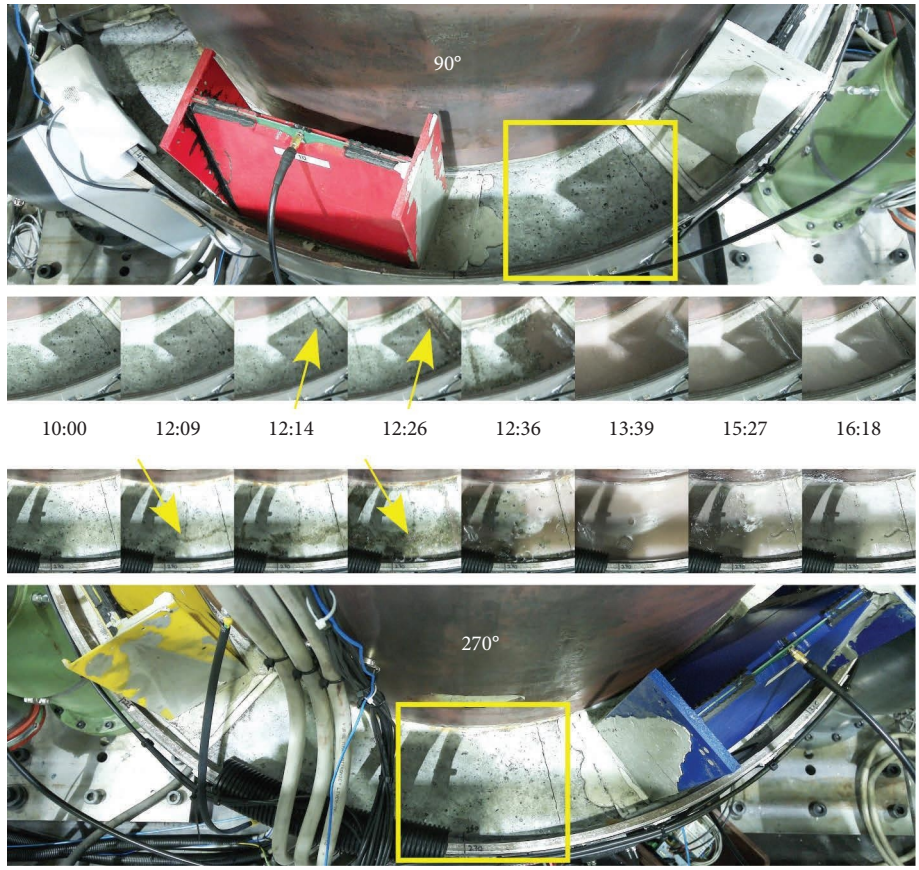

Figure 11: Evolution of the visible damage on November 22 at two opposite sides of the demonstrator (90° and 270°). Small radial surface cracks are visible immediately after curing, with a wet circumferential crack appearing at the 270° position by 12:09 UTC (indicated by a yellow arrow). At 12:14 UTC, water starts escaping from one of the radial cracks at the 90° position. At 12:26 UTC, a growing volume of water surfaced from the cracks, gradually filling the area above the grout, leaving only the water surface visible. The water surface remains visible until 15:27 UTC when most of it disappears, leaving the surface still wet. At 16:18 UTC, the surface dries up further.

$$W = \int F \mathrm{d}s, \tag{2}$$

where W represents the work done by force F and ds is the infinitesimal displacement. Another approach is to calculate the Pearson product-moment correlation coefficient (see (3)), which in this case measures the linear relationship between force and displacement. It spans from −1 to 1, where −1 denotes a perfect negative correlation, 0 represents no correlation, and 1 indicates a perfect positive correlation.

$$r_{ab} = \frac{\sum_{i=1}^{n} (a_i - \overline{a})(b_i - \overline{b})}{\sqrt{\sum_{i=1}^{n} (a_i - \overline{a})^2 \sum_{i=1}^{n} (b_i - \overline{b})^2}}, \tag{3}$$

where n denotes the sample size, a_i and b_i are the individual sample points, and $\overline{a}$ and $\overline{b}$ are their arithmetic mean. Both methods aid in visualizing the progression of damage in the structure from the perspective of the hydraulic system.

Figure 13 illustrates the evolution of work and correlation coefficient for all four days of hydraulic loading. It is important to note that the data can only be compared within each load level and not across different levels. The damage depicted in Figure 11 can also be observed in Figure 13. It is evident that only on the fourth day major damage occurred to the grouted connection because the work and correlation coefficient changed significantly during the fatigue test while on the other days no meaningful change was observed. This is likely because the initial small cracks in the grout only became gradually larger after a significant number of load cycles and then propagated. Initially, the grout and steel structure maintain their full integrity as long as the steel does not reach the plasticized state and the concrete's compressive strength is not locally exceeded. The only conceivable immediate damage is that the concrete in the tension area initially adhered to the steel and then rapidly separated from it. Concrete has limited resistance to tensile forces but can withstand high compressive loads.

3.3. Results of Radar Signal Processing. The results of the radar measurements conducted for all combinations of transmitting (Tx) and receiving (Rx) antennas are shown in Figure 14. The presence of gray signifies instances when laboratory staff was likely present. The presence of people should be taken into account when analyzing the radar data as their movements and equipment operation could influence the radar measurements. These periods were identified by analyzing camera images during times when the ceiling

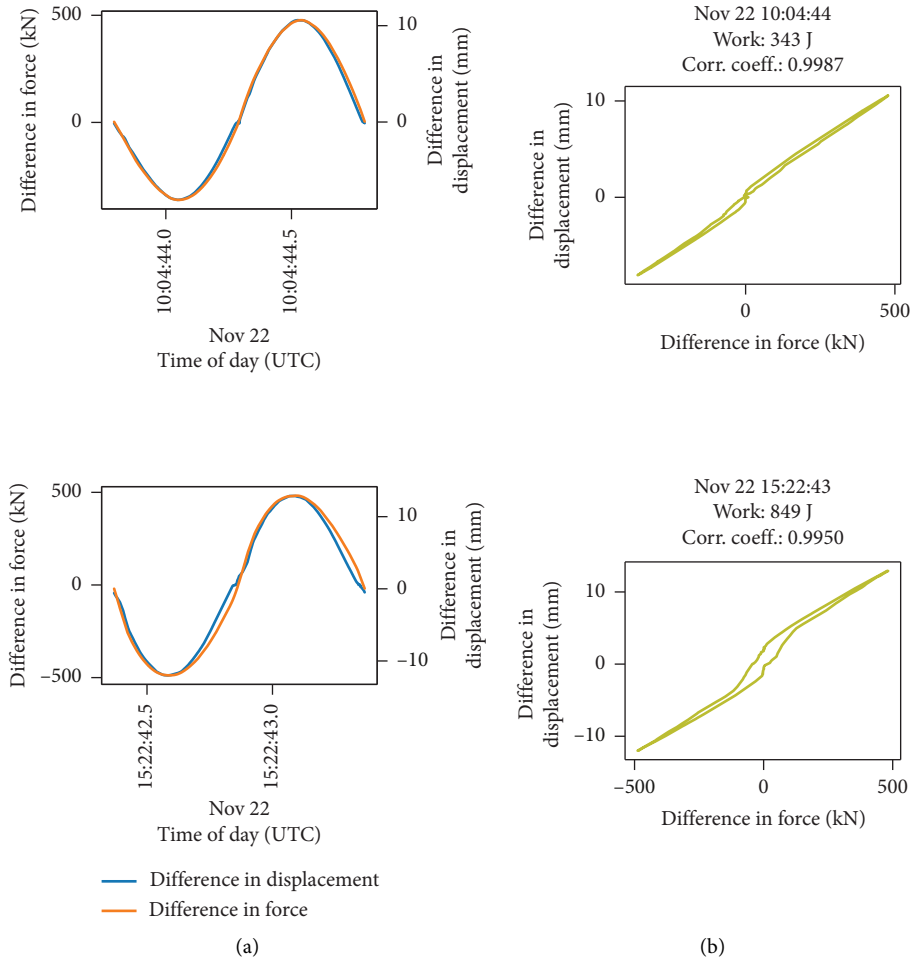

Figure 12: Comparison of force and displacement of the hydraulic cylinders at the beginning and end of November 22 (as time/force and time/displacement plot (a) and force/displacement plot (b)).

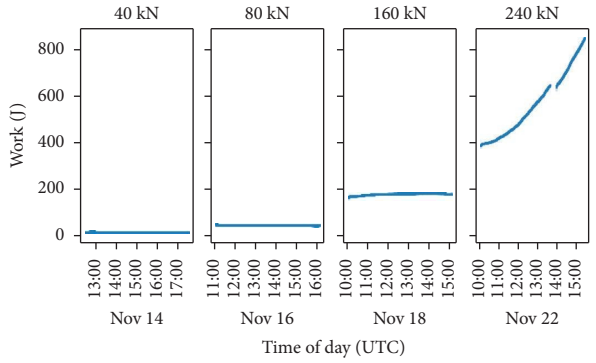

Figure 13: Continued.

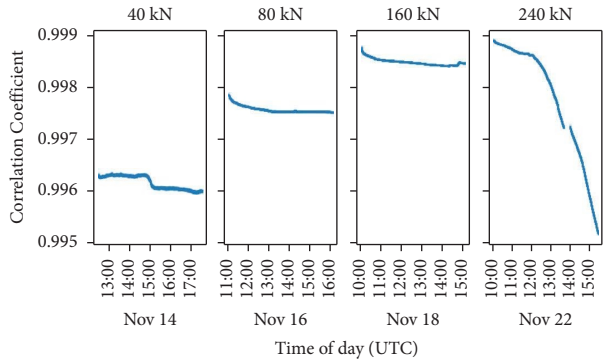

(b)

FIGURE 13: Work (integral of the force/displacement curve) (a) and Pearson product-moment correlation coefficient of force and displacement (b).

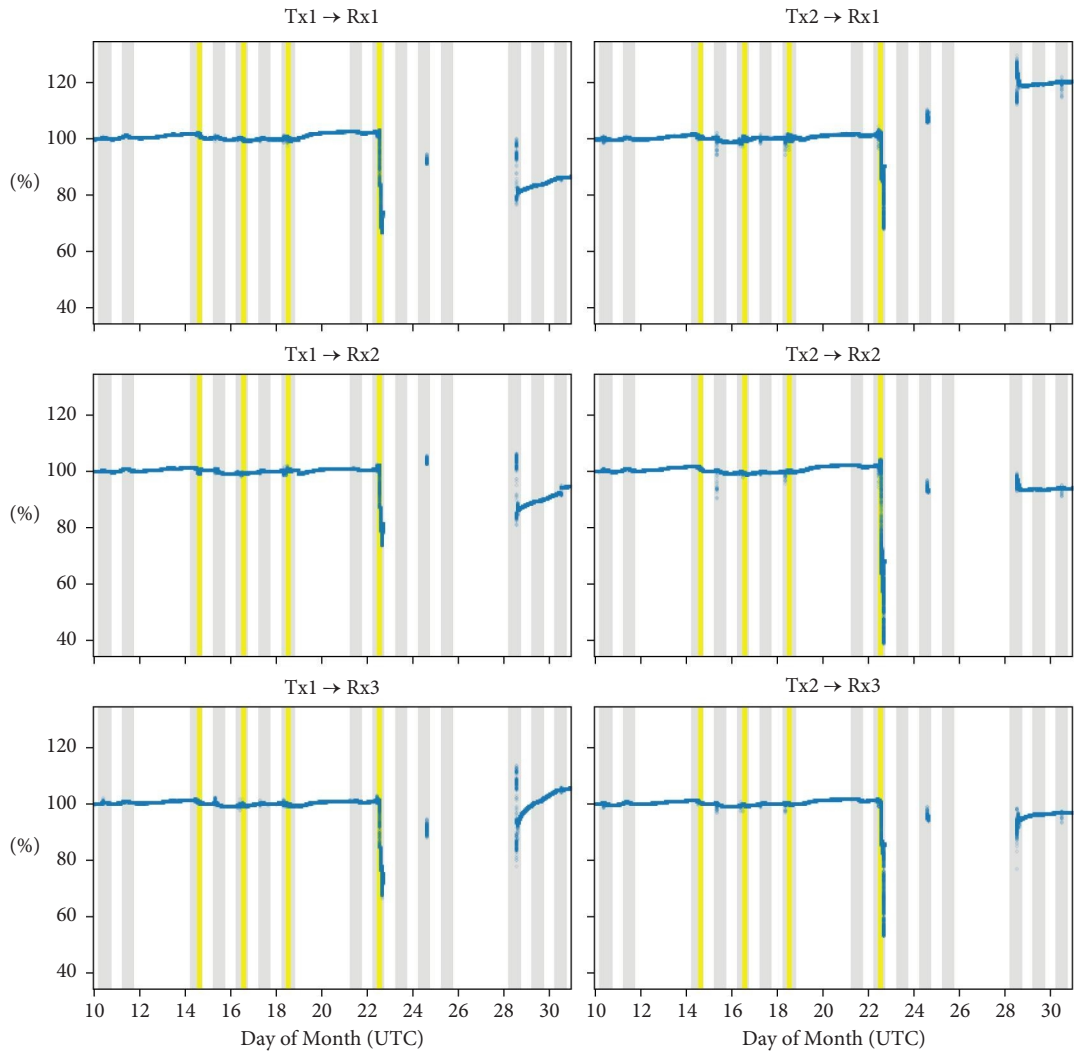

FIGURE 14: Results of the radar measurements for all antenna combinations. Gray indicates the times when staffs were present in the laboratory. Yellow indicates the times of the fatigue test.

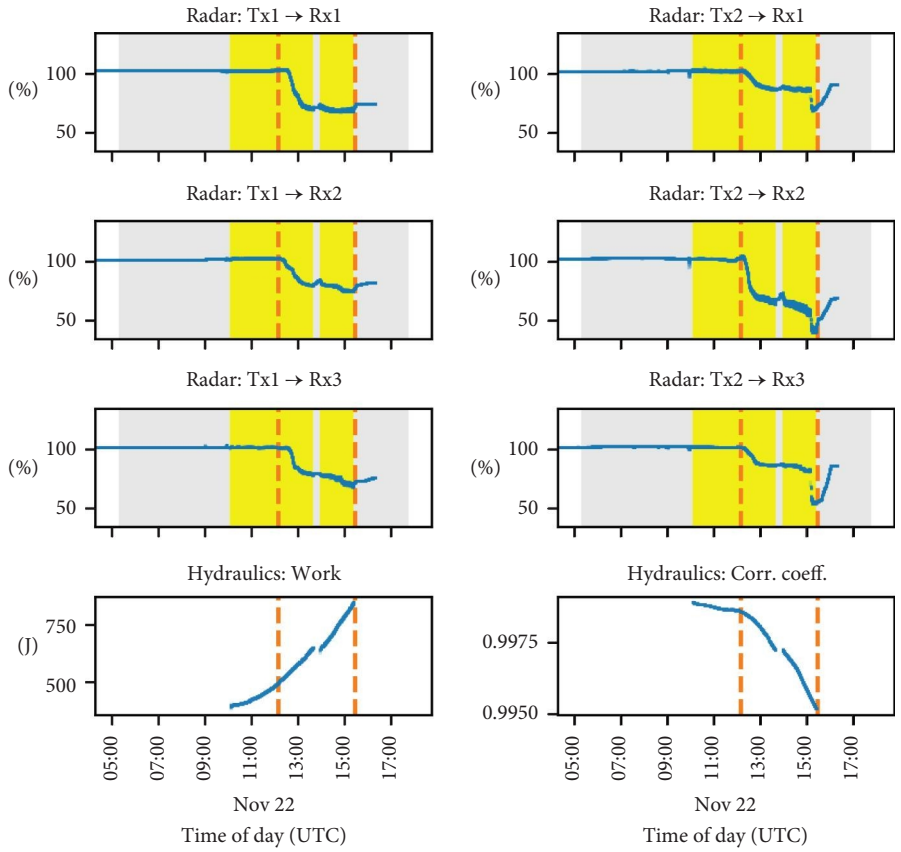

Figure 15: Results of the radar measurements for all antenna combinations on November 22. Gray indicates the times when staffs were present in the laboratory. Yellow indicates the times of the fatigue test. The dashed line shows the first visual appearance of water on the surface of the grout and the disappearance of the water (although the surface was still wet afterwards).

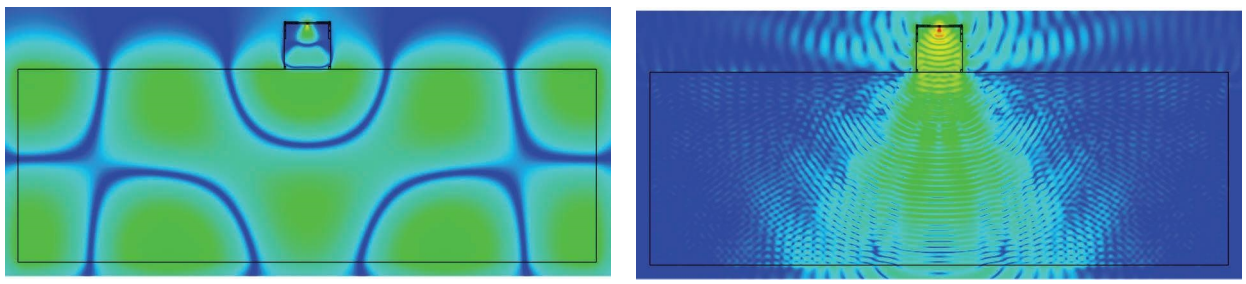

(a) (b)

Figure 16: Simulation of the E-field of one antenna placed on the grouted connection at 100 MHz (a) and 2 GHz (b). The black rectangle shows the boundary of the metal/grout area.

lights were turned on. Consequently, no gray periods are indicated during weekends. The yellow areas indicate the periods during which the fatigue test was performed.

The radar sensor successfully detected the major damage. It is evident from the figure that significant damage occurred exclusively on November 22. Therefore, the radar observed consistent properties initially, followed by rapid changes on November 22. Figure 15 provides a detailed plot of the radar measurement results for all antenna combinations specifically on that day. Additionally, one dashed line is incorporated in the figure to visually indicate the initial appearance of water on the grout surface. Another dashed line marks the point in time after which most of the water had flown back into the cracks. But the surface stayed wet and afterwards gradually dried over time.

The dielectric properties of the dry grout were examined in [31]. During the fatigue test the properties of the grout are not homogeneous, since it partly contains water rising in the grouted connection. Thus, a precise localization of the damage must consider this inhomogeneity. In addition, the electromagnetic waves can propagate over several paths from the transmitter to the damage and back to the receiver,

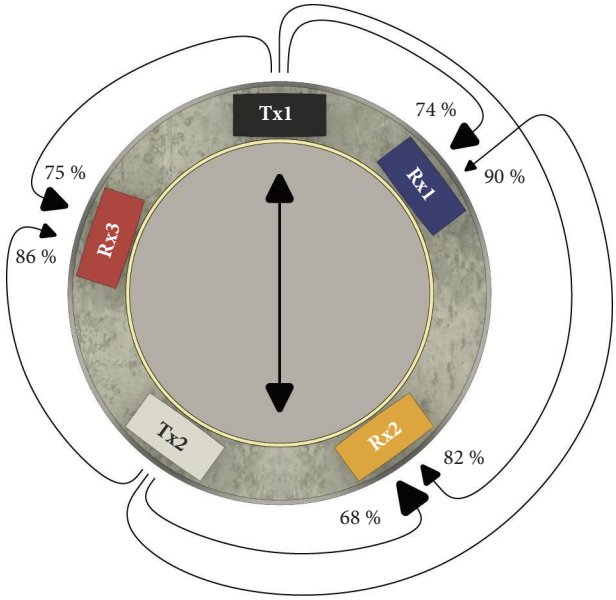

FIGURE 17: Values of the last radar measurement on November 22 at 16:18 UTC in relation to the position of the antenna combination on the grouted connection.

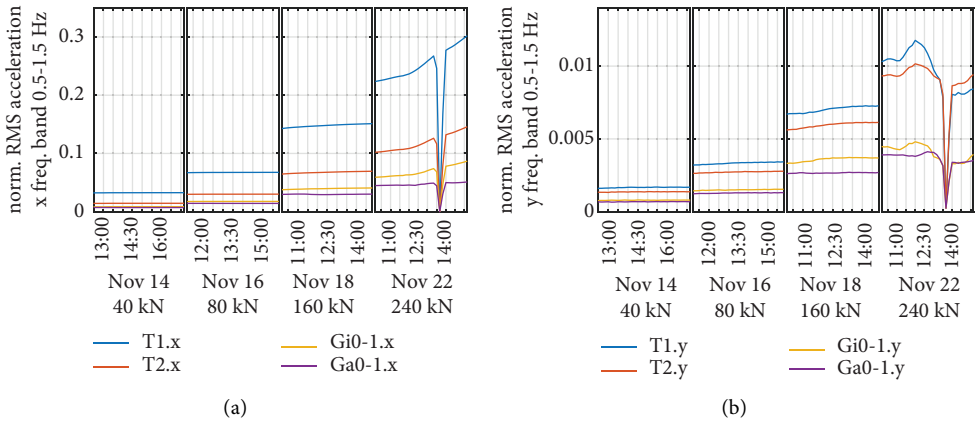

FIGURE 18: Normalized RMS values of acceleration in the frequency band 0.5–1.5 Hz in load direction (a) and transverse to load direction (b) measured by four MEMS acceleration sensors at the measurement positions T1, T2, Gi0-1, and Ga0-1 during hydraulic excitation at four load levels.

e.g., on a straight path or around the circumference. Figure 16 showcases a simulation of the electric field (E-field) in the grouted connection using the CST Microwave Studio for a single antenna. The cylindrical shape of the demonstrator was unwrapped to enable simulation and plotting of the data. The top and bottom sections correspond to different frequencies: 100 MHz and 2 GHz. The simulation provides insight into the distribution and behavior of the E-field in relation to the grouted connection at these specific frequencies. The different wavelengths corresponding to the lower and higher frequency can be easily observed. The simulation results illustrate why a rough estimation of the damage position can be possible. At low frequencies, the electric field of the transmitting antenna spreads throughout the whole demonstrator, while at higher frequencies, the signal tends to be more concentrated below the antenna.

The values obtained from the last radar measurement conducted on November 22 at 16:18 UTC (see Figure 15) are presented in Figure 17 with an arrow indicating the location of the corresponding transmitting and receiving antenna. The reduction of the damage indicator after the damage event is location-dependent. The largest change occurred between Tx2 and Rx2, which was also one of the areas where the finite element analysis (see Figure 2(b)) predicted the

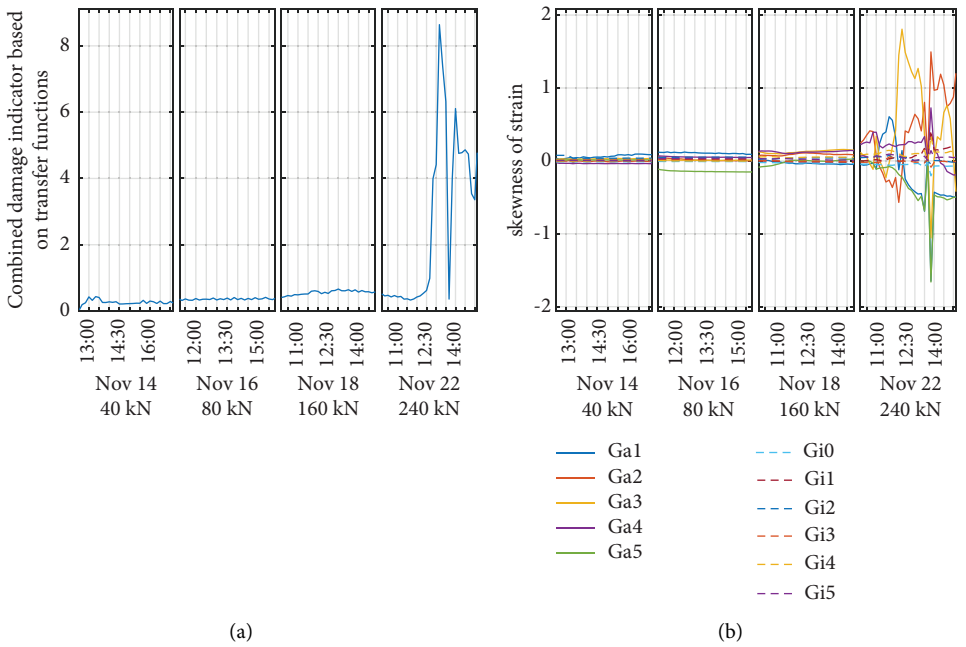

FIGURE 19: Transfer function-based damage indicator (a) and skewness of strain signals (b) during hydraulic excitation at four load levels and the measurement positions Ga1-Ga5 at the outer pipe resp. Gi0-Gi5 at the inner pipe.

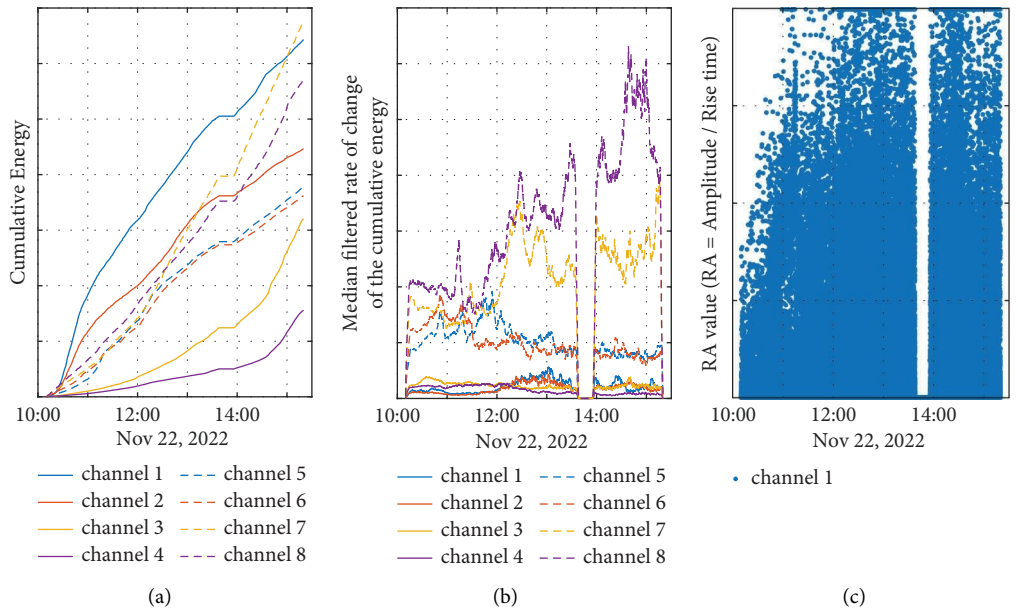

FIGURE 20: Cumulative energy (a), median filtered rate of change of the cumulative energy (b), and RA value (c) of acoustic emission events.

highest stress beforehand. A rough localization of the damage in relation to the circumference of the grouted connection is therefore possible based on the antenna positions.

3.4. Vibration Analysis. A large number of sensors for vibration and acoustic emission measurement were installed on the laboratory demonstrator from outside and inside. These enabled versatile monitoring of the grout and finally damage detection using global and local methods. In this paper, only a small insight to this field is provided. A total of 100 measurement channels were recorded by means of two measurement systems: 64 strain gauge channels distributed over the height and circumference of the grouted joint, six Pt100 temperature sensors for temperature measurement and compensation, four triaxial micro-electro-mechanical-system (MEMS) acceleration sensors on different levels of the test rig, two uniaxial MEMS acceleration sensors on the shaker, two

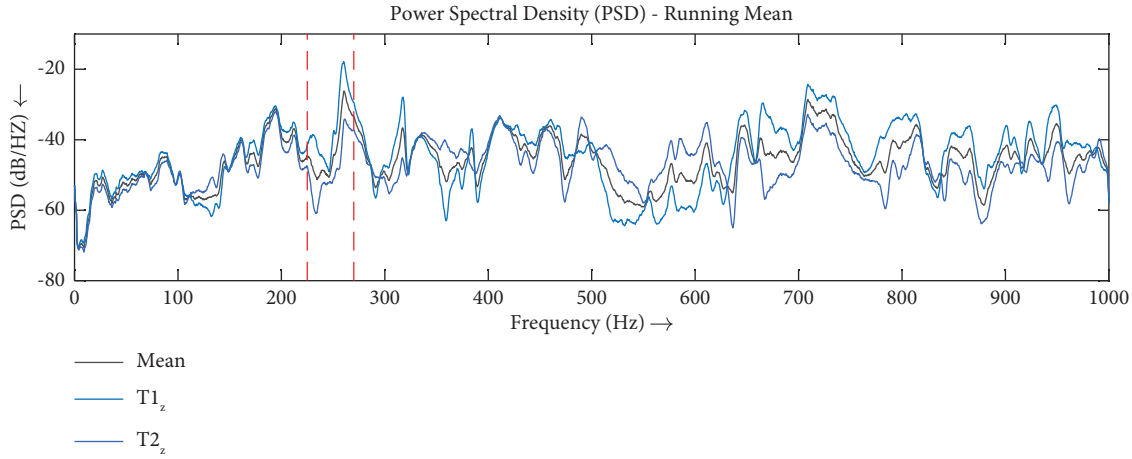

Figure 21: PSD over the whole frequency range. The red dashed lines show as an example the range of interest for the modal analysis.

Table 4: Evaluation of the modal analysis of damage mode.

Date	Associated load level	Frequency (Hz)	Diff. to previous (Hz)	Damping (%)	Diff. to previous (%)
October 31	Reference	260.41	—	0.5	—
November 03	Initial commissioning 10%	258.46	−1.95	0.52	0.02
November 16 08:36 UTC	5 hours 10%	254.43	−4.03	1.02	0.5
November 18 07:36 UTC	5 hours 20%	251.72	−2.71	1.37	0.35
November 22 07:36 UTC	5 hours 40%	247.59	−4.13	2.93	1.56

piezo acceleration sensors, three force and displacement sensors each in the hydraulic cylinders, and eight acoustic emission sensors.

Using various evaluation methods, the damage state of the test rig can be continuously monitored. One of the global methods is the operational modal analysis (OMA); some results are presented in the next section. However, even statistical features already allow the damage progress to be identified. For example, in Figure 18, the normalized RMS values of acceleration in the frequency band from 0.5 to 1.5 Hz show not only a step-like increase in the values due to the step-wise increasing load levels, but also a change during the respective load levels. These indicate a change in the structural properties, especially the reduction of structural stiffness, caused by the hydraulic excitation and thus a change in the frequency spectrum of the acceleration signals. It is also interesting to note that the properties also change transversely to the load direction and that these can also be measured. The large short-term change in all the curves on November 22 at about 13:40 UTC results from a short switch-off of the test rig.

The significant damage progress during the fourth load stage can be clearly recognized using both, the more global acceleration measurement and the more local strain measurement. As an example, this is shown in Figure 19 using an indicator based on the combination of transfer functions between multiple strain gauges as well as the skewness for selected strain gauge channels [34]. A clear change in the characteristics and indicators can be seen, in particular on November 22 starting from approx. 12:00 UTC.

This significant damage progress can also be observed by acoustic emission analysis. This can be seen impressively in Figure 20, for example, in the increasing cumulative energies [35] and their rates of change for the individual sensors. Features such as the RA value, which is the ratio of amplitude and rise time (see (4)), show corresponding changes. The different rates of change of the acoustic emission energy for the individual sensor channels are already an indication for local accumulations of the acoustic emission sources in the laboratory structure.

$$\mathrm{RA} = \frac{\text{Amplitude}}{\text{Rise time}}. \tag{4}$$

The visual observations (see previous section) correspond to the findings from the continuous evaluation of the (local) vibration signals as well as the results of the acoustic emission analysis, so that it is possible to monitor both long-term trends and transient damage events, respectively.

3.5. Modal Analysis. An important and powerful tool for damage detection in the field of vibration analysis is the OMA. There are various well-known techniques, which can be used, each with its own advantages and disadvantages [36]. Here, a modified approach of the stochastic subspace identification covariance driven algorithm (SSI-COV OMA) was used to analyze the acceleration data [37]. The acceleration was recorded by MEMS sensors during the structure was excited by an electrohydraulic shaker. The excitation procedure was triggered before each hydraulic load level, in order to track the modal quantities of the laboratory

demonstrator. The frequency range of the random excitation was relatively high (up to 1000 Hz) and could therefore excite as many modes as possible.

Figure 21 shows the PSD from two channels of accelerometer sensors measuring parallel to the shaker excitation. $T1$ and $T2$ denote the acceleration sensors and z is the corresponding measuring direction. The red dashed lines show the frequency range where a dominant mode is sensitive to damage. This frequency range has been selected for further analysis. To smooth the results of the PSD, a running mean filter was used in this case for display purposes only.

According to the results of the OMA as given in Table 4, a clear reduction of the eigenfrequency and an increase of damping are a definite indication for the damage manifested as a decrease of the structural stiffness and an increase of the friction in the grout. A degradation of the grouted connection had already occurred after the first load level. No plastic deformation was observed in the steel components, suggesting that the damage was confined to the grout material itself. The suspicion was confirmed as the load level was increased, with the appearance of cracks in the grouted joint.

4. Conclusions

This paper presented an innovative approach for in situ monitoring of the grouted connection in offshore wind turbines using a stepped-frequency continuous wave (SFCW) radar. The proposed radar-based structural health monitoring system offers a nondestructive and real-time method for assessing the structural integrity of the grouted connection directly, actively, and automatically. Through a newly developed large-scale experiment and subsequent fatigue testing, the effectiveness of the radar approach was demonstrated. A rough localization of the damage in relation to the circumference of the grouted connection was possible based on the antenna positions.

For validation, this study also presented visual observations, hydraulic cylinder data, vibration analysis, acoustic emission analysis, and modal analysis. These results confirm the radar system's ability to detect damage in the grouted connection and effectively monitor the integrity of the turbine foundation. By providing real-time information on the structural health, the proposed approach can enable predictive maintenance strategies and the optimization of the operational lifetime as well as a reduction of maintenance cost of offshore wind turbines in the future.

Data Availability

The experimental data used to support the findings of this study are available from the corresponding author upon request.

Conflicts of Interest

The authors declare that they have no conflicts of interest regarding the publication of this paper.

Acknowledgments

The authors gratefully acknowledge the financial support of this research by the Federal Ministry for Economic Affairs and Climate Action (Grant nos. 03EE3023A, 03EE3023B, 03EE3023C, and 03EE3023D). Open Access funding was enabled and organized by Projekt DEAL.

Supplementary Materials

The following link shows the video clip of the time-lapse sequence of visible damage development on November 22 similar to Figure 11 but with more details: https://w.wiki/7AGK. The observations were made on the demonstrator from two opposite sides, namely, 90° and 270°. Initially, after the demonstrator was cured, small radial surface cracks were visible. During the time-lapse, circumferential cracks appear and water escapes from the cracks. The water subsequently fills the volume above the grout until only the water surface is visible. After the fatigue test is completed for this day, the water mostly disappears from the surface, although the grout at first remains wet. Afterwards, the grout slowly dries, but the deposition of pulverized grout sediment remains on the existing grout surface as a new layer giving the grout a smooth appearance. (*Supplementary Materials*)

References

[1] Global Wind Energy Council, "Global wind report 2023," 2023, https://gwec.net/wp-content/uploads/2023/03/GWR-2023_interactive.pdf.

[2] European Commission, "An EU Strategy to harness the potential of offshore renewable energy for a climate neutral future," European Commission, Brussels, Belgium, COM/2020/741, 2020.

[3] M. Vieira, E. Henriques, B. Snyder, and L. Reis, "Insights on the impact of structural health monitoring systems on the operation and maintenance of offshore wind support structures," *Structural Safety*, vol. 94, Article ID 102154, 2022.

[4] L. Wang, A. Kolios, X. Liu, D. Venetsanos, and R. Cai, "Reliability of offshore wind turbine support structures: a state-of-the-art review," *Renewable and Sustainable Energy Reviews*, vol. 161, Article ID 112250, 2022.

[5] T. Maetz, M. Hägelen, R. Jetten et al., "In-situ monitoring of grouted joints using a SFCW radar: initial results of an installation inside a 3.6 MW offshore wind turbine," in *Proceedings of the 2023 17th European Conference on Antennas and Propagation (EuCAP)*, pp. 1–5, IEEE, Florence, Italy, March, 2023.

[6] C. R. Brett, D. A. Gunn, B. A. J. Dashwood, S. J. Holyoake, and P. B. Wilkinson, "Development of a technique for inspecting the foundations of offshore wind turbines," *Insight- Non-Destructive Testing and Condition Monitoring*, vol. 60, no. 1, pp. 19–27, 2018.

[7] E. Sørensen, L. Westhof, E. Yde, and A. Serednicki, "Fatigue life of high performance grout for wind turbine grouted connection in wet or dry environment," in *Proceedings of the Poster presented at EWEA OFFSHORE 2011*, Amsterdam, Netherlands, December 2011.

[8] P. Schaumann, J. Henneberg, A. Raba, L. Lohaus, and D. Cotardo, *Überwiegend axial wechselbeanspruchte Grout-Verbindungen in Tragstrukturen von Offshore-*

Windenergieanlagen, Gottfried Wilhelm Leibniz Universität Hannover, Hanover, Germany, 2018.

[9] N. Tziavos, "Experimental and numerical investigations on grouted connections for monopile offshore wind turbines," Doctoral thesis, University of Birmingham, Birmingham, UK, 2019.

[10] J. Shan, L. Wang, C. N. Loong, and Z. Zhou, "Rapid seismic performance evaluation of existing frame structures using equivalent SDOF modeling and prior dynamic testing," *Journal of Civil Structural Health Monitoring*, vol. 13, pp. 749–766, 2023.

[11] S. B. Lendve, G. C. Enss, S. Tsiapoki, C. Ebert, and J. Asmussen, "Probabilistischer Ansatz zur Detektion von Strukturveränderungen an Monopile-Gründungsstrukturen mit Messdaten aus einem Structural Health Monitoring System," *Stahlbau*, vol. 89, no. 6, pp. 542–550, 2020.

[12] B. Stuyts, W. Weijtjens, M. Gkougkoudi-Papaioannou, C. Devriendt, P. Troch, and A. Kheffache, "Insights from in-situ pore pressure monitoring around a wind turbine monopile," *Ocean Engineering*, vol. 269, Article ID 113556, 2023.

[13] J. Shan, C. Zhuang, and C. N. Loong, "Parametric identification of Timoshenko-beam model for shear-wall structures using monitoring data," *Mechanical Systems and Signal Processing*, vol. 189, Article ID 110100, 2023.

[14] F. Liu, Q. Yu, H. Li, Y. Zhan, H. Zhou, and D. Liu, "Field data observations for monitoring the impact of typhoon "In-fa" on dynamic performances of mono-pile offshore wind turbines: a novel systematic study," *Marine Structures*, vol. 89, Article ID 103373, 2023.

[15] N. Müller, P. Kraemer, D. Leduc, and F. Schoefs, "FBG sensors and signal-based detection method for failure detection of an offshore wind turbine grouted connection," *International Journal of Offshore and Polar Engineering*, vol. 29, no. 1, pp. 1–7, 2019.

[16] M. W. Häckell, H. Friedmann, and M. Feulner, "Detecting damage in grouted-joints of wind turbine support structures-application to a large-scale experiment," in *Proceedings of the 11th International Workshop on Structural Health Monitoring*, pp. 2467–2474, Stanford, CA, USA, September 2017.

[17] B. Weihnacht, T. Gaul, R. Neubeck et al., "Groutüberwachung an Offshore-Windenergieanlagen mit geführten Wellen," in *Proceedings of the DGZfP-Jahrestagung*, Koblenz, Germany, May 2017.

[18] J. Moll, "Damage detection in grouted connections using electromechanical impedance spectroscopy," *Proceedings of the Institution of Mechanical Engineers- Part C: Journal of Mechanical Engineering Science*, vol. 233, no. 3, pp. 947–950, 2019.

[19] E. Hammarström, "Non-destructive testing of concrete with ground penetrating radar," 2018, https://www.diva-portal.org/smash/record.jsf?pid=diva2:1280320.

[20] A. M. Alani, M. Aboutalebi, and G. Kilic, "Applications of ground penetrating radar (GPR) in bridge deck monitoring and assessment," *Journal of Applied Geophysics*, vol. 97, pp. 45–54, 2013.

[21] M. Ata, M. Abouhamad, M. Hassanien Serror, and M. Marzouk, "Data acquisition and structural analysis for bridge deck condition assessment using ground penetration radar," *Journal of Performance of Constructed Facilities*, vol. 35, no. 5, 2021.

[22] Z. W. Coleman and A. K. Schindler, "Investigation of ground-penetrating radar defect detection capabilities, influence of moisture content, and optimal data collection orientation in condition assessments of concrete bridge decks," *Journal of Applied Geophysics*, vol. 202, Article ID 104655, 2022.

[23] F. Chen, X. Jia, J. Xu, and J. Wu, "Research on nondestructive detection and trenchless treatment of abutment slab void," in *Advances in Frontier Research on Engineering Structures*, pp. 654–660, CRC Press, Boca Raton, FL, USA, 2023.

[24] H. Latif, "Ground-penetrating radar (GPR) for non-destructive characterization of reinforced concrete structures," 2023, https://urn.fi/URN:NBN:fi:aalto-202301291790.

[25] E. C. Oikonomopoulou, V. A. Palieraki, I. P. Sfikas, and C. G. Trezos, "Reliability and limitations of GPR for identifying objects embedded in concrete– experience from the lab," *Case Studies in Construction Materials*, vol. 16, Article ID e00898, 2022.

[26] M. Abdul Rahman, D. Donda, F. Latosh, A. Tarussov, and A. Bagchi, "Entropy evaluation of subsurface materials and defects in Concrete Slabs using GPR," in *Proceedings of the 11th International Conference on Structural Health Monitoring of Intelligent Infrastructure*, Montreal, Canada, August 2022.

[27] W. Wai-Lok Lai, X. Dérobert, and P. Annan, "A review of ground penetrating radar application in civil engineering: a 30-year journey from locating and testing to imaging and diagnosis," *NDT & E International*, vol. 96, pp. 58–78, 2018.

[28] J. Kappel, M. Wiemann, J. Käsgen et al., "Development and installation of a robust and reliable research structural health monitoring system for grouted joints of offshore wind turbines," in *Proceedings of the 2023 14th International Workshop on Structural Health Monitoring*, IWSHM, Stanford, CA, USA, September 2023.

[29] Pagel Spezial-Beton GmbH & Co Kg, "Technical data sheet: PAGEL HF10 super-high-strength grout (C80/95)," https://www.pagel.com/all/pdf/gb/hf10_gb.pdf.

[30] Bosch Sensortec GmbH, "Data sheet: BME280 (Digital humidity, pressure and temperature sensor)," https://www.bosch-sensortec.com/media/boschsensortec/downloads/datasheets/bst-bme280-ds002.pdf.

[31] T. Maetz, M. Hägelen, R. Jetten, and J. Moll, "Detection of water through steel-lined grout using a stepped-frequency continuous wave radar," in *Proceedings of the 2022 16th European Conference on Antennas and Propagation (EuCAP)*, pp. 1–4, IEEE, Madrid, Spain, March, 2022.

[32] J. Simon, T. Kurin, J. Moll et al., "Embedded radar networks for damage detection in wind turbine blades: validation in a full-scale fatigue test," *Structural Health Monitoring*, vol. 22, no. 6, pp. 4252–4263, 2023.

[33] M. Kohlmeier, S. Spill, M. Häckell, A. Schenk, and H. Friedmann, *Physikalische Modellversuche an Monopile-Tragstrukturen mit Grout-Verbindungen zur Bewertung von Structural-Health-Monitoring-Systemen*, Fraunhofer-Gesellschaft, Munich, Germany, 2018.

[34] T. J. Johnson and D. E. Adams, "Transmissibility as a differential indicator of structural damage," *Journal of Vibration and Acoustics*, vol. 124, no. 4, pp. 634–641, 2002.

[35] European Committee for Standardization, *EN 1330-9:2017-10– Non-destructive Testing– Terminology– Part 9: Terms Used in Acoustic Emission Testing*, European Committee for Standardization, Brussels, Belgium, 2017.

[36] J.-H. Yi and C.-B. Yun, "Comparative study on modal identification methods using output-only information," *Structural Engineering & Mechanics*, vol. 17, 2004.

[37] M. Wiemann, L. Bonekemper, J. Kappel, and P. Kraemer, "Separation of physical from mathematical poles in operational modal analysis using reduced, reassembled covariance matrices," in *Proceedings of the 2023 14th International Workshop on Structural Health Monitoring*, IWSHM, Stanford, CA, USA, September 2023.